

Site-wise manipulations and Mott insulator-superfluid transition of interacting photons using superconducting circuit simulators

Xiuhao Deng,¹ Chunjing Jia,^{2,3} and Chih-Chun Chien^{1,*}

¹*School of Natural Sciences, University of California Merced, Merced, California 95343, USA*

²*Department of Applied Physics, Stanford University, California 94305, USA*

³*Stanford Institute for Materials and Energy Sciences, SLAC National Accelerator Laboratory, 2575 Sand Hill Road, Menlo Park, California 94025, USA*

(Dated: November 15, 2021)

The Bose Hubbard model (BHM) of interacting bosons in a lattice has been a paradigm in many-body physics, and it exhibits a Mott insulator (MI)-superfluid (SF) transition at integer filling. Here a quantum simulator of the BHM using a superconducting circuit is proposed. Specifically, a superconducting transmission line resonator supporting microwave photons is coupled to a charge qubit to form one site of the BHM, and adjacent sites are connected by a tunable coupler. To obtain a mapping from the superconducting circuit to the BHM, we focus on the dispersive regime where the excitations remain photon-like. Standard perturbation theory is implemented to locate the parameter range where the MI-SF transition may be simulated. This simulator allows single-site manipulations and we illustrate this feature by considering two scenarios where a single-site manipulation can drive a MI-SF transition. The transition can be analyzed by mean-field analyses, and the exact diagonalization was implemented to provide accurate results. The variance of the photon density and the fidelity metric clearly show signatures of the transition. Experimental realizations and other possible applications of this simulator are also discussed.

PACS numbers: 42.50.Pq, 05.30.Jp, 74.81.Fa, 02.70.-c

I. INTRODUCTION

Intense research has been focused on simulating complex matter using well-controlled quantum systems in order to better understand their behavior and create useful analogues^{1-5,10}. Successful examples include cold atoms trapped in optical potentials², trapped ions^{1,4}, spins in defects in diamonds⁵, photonic arrays³, etc. Recently, another class of quantum simulators based on superconducting circuits opens more opportunities^{6-9,13}, which is made possible due to progresses in fabricating well-designed circuits on chips. In those superconducting circuits, dissipation and decoherence have been suppressed significantly^{13,45}. Moreover, interacting superconducting qubits or resonators can be fabricated on a chip, where quantum error-correction encoding and high fidelity operations have been realized^{16,17}. Various designs of couplers for connecting different qubits or resonators with wide tuning ranges have also been demonstrated^{49,50,52}. Those progresses in superconducting circuits provide a promising perspective of scalable superconducting circuits as quantum simulators for many-body systems, which may be bosonic^{6,18,32,40} or fermionic^{37,38} in nature.

The Bose-Hubbard Model (BHM) has been a paradigm in many-body theories, and the Mott insulator-superfluid (MI-SF) phase transition associated with the BHM has been of broad interest^{2,19}. This transition was observed unambiguously in cold atoms trapped in optical lattices and can be probed with single-atom resolutions^{23,24}. On the other hand, a theoretical framework for obtaining the BHM using the Jaynes-Cummings Hubbard Model has been established^{27,28}. Simulating this general model in cavity arrays has been proposed^{22,25-27}. One may en-

vision that introducing inhomogeneity into the BHM parameters can lead to richer physics, some of which has been explored in Refs. 33,82. Simulating those phenomena requires tunability of single-site parameters, which could be hard in current available simulators^{1,2,4,5,10}.

As a candidate of quantum simulators, superconducting circuit has the following additional features^{6,10,11}: (I) The circuit can be manipulated by applying voltages, currents and/or magnetic flux. Hence useful classical circuit techniques can be introduced in similar ways. (II) Circuit manipulations can be implemented locally to a single site/unit or globally to the whole system. (III) The circuit can be tailored to certain characteristic frequency, interaction strength, etc., and the circuit geometry can be fabricated in desired patterns. Furthermore, according to recent reports the decoherence time of superconducting qubits based on different superconducting circuits is approaching $0.1ms$ ^{44,46,60,61}. The Q factor of an on-chip transmission line resonator⁴³ can even go beyond 10^5 . A 3D superconducting resonator^{45,46} can have a quality factor up to 10^9 , which implies that the life time of photons in superconducting resonators may approach $10ms$. This is good enough to allow one to consider the photon number as a conserved quantity in the circuit if compared to the operation frequency in the circuit typically in the range of $100MHz-10GHz$ ¹¹⁻¹⁴.

Having those features of superconducting circuit in mind, we propose a scheme to simulate the BHM with controllable inhomogeneous parameters. To demonstrate some interesting features, we consider how the phase transition between the delocalized SF and localized Mott insulator can be induced by manipulating the parameters of one single site. In conventional setups, global param-

eters such as the density or interaction drive the system across this transition, and here we propose that in superconducting-circuit simulators, one may observe this transition with a single-site manipulation. The details of our proposed scheme are verified by the exact diagonalization method⁶⁴, which already shows signatures of this transition in moderate-size systems. Thus this proposed scheme should be feasible in experiments.

Here the simulator is based on an array of superconducting transmission line resonators (TLRs). The goal is to simulate the BHM¹⁹

$$H = -\sum_i \mu_i n_i + \sum_i \frac{U_i}{2} n_i (n_i - 1) - \sum_i t_i (b_i^\dagger b_{i+1} + b_i b_{i+1}^\dagger). \quad (1)$$

Here μ_i is the on-site energy and it usually plays the role of the chemical potential, U_i is the on-site interaction, and t_i is the nearest-neighbor hopping coefficient. In cold atoms one can control the filling and motion of a single atom²³, but manipulations of the energy and interaction on each site remain a challenge.

A superconducting TLR with a length in the range of centimeters can support a microwave resonant frequency corresponding to the oscillations of the electric potential and magnetic flux from the standing waves of the Cooper pair density. Those microwaves are referred to as the photons in the TLR³⁰. The quantum electrodynamics (QED) framework can then be applied to the TLR-qubit system to get the so-called circuit QED³⁰. A single site of the system is modeled by the Jaynes-Cummings (JC) model²⁰ while an array of circuit QED systems, as schematically shown in Figure 1, can be described by the Jaynes-Cumming Hubbard model²¹

$$H = \sum_n [\hbar\omega_n^c a_n^\dagger a_n + \hbar\omega^q \sigma_n^z + g_n (a_n \sigma_n^+ + a_n^\dagger \sigma_n^-)] + \sum_n J_n (a_n^\dagger a_{n+1} + a_n a_{n+1}^\dagger), \quad (2)$$

where the parameters are ω_n^c as the cavity frequency, ω^q as the qubit frequency, g_n as the coupling strength between the cavity and qubit, and J_n as the hopping coefficient between cavities.

When the qubit is close to resonance with the cavity, they are co-excited and the excitation on a single site has the form of a polariton. Simulating polaritonic many body behavior has been studied recently based on various physical systems^{32,39,41}. Here we consider a different regime in the parameter space to take advantage of the tunability of superconducting quantum circuits. We focus on the dispersive regime²⁸, where the excitation is limited in the TLR while the qubit stays in its ground state. Hence the on-site excitation becomes photonic. In this regime, a perturbation calculation shows that the system can simulate the BHM. To make connections to experiments, feasible controlling and probing methods of the quantum phase transition between localized and delocalized states will be discussed. The exact diagonaliza-

tion (ED)⁶⁴ method is used to numerically demonstrate the details of the phase transition.

II. ARCHITECTURE OF THE SIMULATOR

As illustrated in Figure 1, the proposed simulator is a one dimensional (1D) array of superconducting circuit elements. One site is formed by a TLR capacitively coupled to a superconducting charge qubit¹¹⁻¹⁴, which is labeled as SQUID-B, and the qubit energy is tunable. The TLRs on different sites are connected via the SQUID-B, which leads to tunable couplings between nearest neighbor sites. Here a derivation of how the Bose-Hubbard Hamiltonian (1) can be simulated by the superconducting circuit will be presented. In order to simplify the derivation, we will use $\text{Hz} \times 2\pi$ as the unit of energy and set $\hbar \equiv 1$.

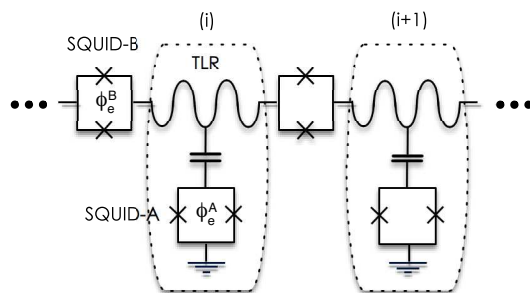


FIG. 1: Schematic plot of the 1D TLR array. SQUID-A as a tunable charge qubit is capacitively coupled to the center of a TLR. Nearest neighbor sites are connected by SQUID-B. The external magnetic flux ϕ_e^A and ϕ_e^B through SQUID A and B can be used to tune their Josephson energies.

A. TLR as a lattice element

The qubit-TLR system is an analogue of an atom-cavity system. In quantum optics the dynamics of the latter system can be modeled by the Janes-Cummings Hamiltonian³⁰. Our superconducting circuit Hamiltonian can be derived following the work of circuit-QED in Refs.²⁹⁻³¹. The Hamiltonian of a single lattice site is

$$H^{site} = H^{TLR} + H^{qubit}. \quad (3)$$

The TLR with length D could be treated as a cavity with a single mode of the first harmonic. Thus

$$\begin{aligned} H^{TLR} &= \frac{(2e)^2}{2C^c} N^2 + \frac{1}{2L^c(2e)^2} (\phi^c)^2 \\ &= \frac{1}{2} E_c^c N^2 + \frac{1}{2} E_L^c (\phi^c)^2 \\ &= \omega^c a^\dagger a, \end{aligned} \quad (4)$$

where the cavity frequency $\omega^c = \frac{2\pi}{\sqrt{C^c L^c}} = 2\pi \sqrt{E_c^c E_L^c}$, the net capacitance of the TLR is C^c , the charge energy

of the cavity $E_c^c = \frac{(2e)^2}{C_c}$, the net inductance of the TLR is L^c and after second quantization, the inductive energy of the cavity is $E_L^c = \frac{1}{L^c(2e)^2}$. The node charge number and node flux at the maximum points become

$$\begin{cases} N = \sqrt{\omega^c/E_c^c}(a^\dagger + a) \\ \phi^c = -i\sqrt{\omega^c/E_L^c}(a^\dagger - a) \end{cases}. \quad (5)$$

For the first harmonic, the spatial distribution³⁰ of N is $\cos(\frac{\pi}{D}x)$, $x \in [-\frac{D}{2}, \frac{D}{2}]$, so the maximum points are $x = -\frac{D}{2}, 0, \frac{D}{2}$ corresponding to the center and two ends of the TLR. Since the qubit consists of two Josephson junctions in a superconducting loop, the qubit Hamiltonian includes the capacitive energy and inductive energy as

$$H^{qubit} = E_c^A(n - n_g)^2 + 2E_J^A \cos(\frac{\phi_e^A}{2})(1 - \cos \phi). \quad (6)$$

Here $n = C_\Sigma^A V_J/2e$ is the number of Cooper pairs on the island and $n_g = C_g^A V_g/2e$ is the number of Cooper pairs on the gate, which has a capacitance C_g^A between the qubit and TLR. $E_c^A = \frac{(2e)^2}{2C_\Sigma^A}$ with C_Σ^A being the total effective capacitance in the qubit. The Josephson tunneling energy is E_J^A and the phase ϕ displaces the number of Cooper pairs. Casting the Hamiltonian in Fock space and dropping the constant term $2E_J^A \cos(\frac{\phi_e^A}{2})$, one obtains

$$H^{qubit} = \sum_n [E_c^A(n - n_g)^2 |n\rangle \langle n| + 2E_J^A \cos(\frac{\phi_e^A}{2})(|n\rangle \langle n+1| + |n+1\rangle \langle n|)]. \quad (7)$$

Because of the giant Kerr effect due to the Josephson junction, the energy difference between the lowest two levels is separated from the other energies. Therefore the SQUID-A can be considered as a superconducting qubit¹¹, where the Pauli matrices are

$$\tilde{\sigma}^x = |0\rangle \langle 1| + |1\rangle \langle 0| \quad (8)$$

$$\tilde{\sigma}^z = -|0\rangle \langle 0| + |1\rangle \langle 1|. \quad (9)$$

Then we obtain

$$H^{qubit} = E_c^A \frac{1 - 2n_g}{2} \tilde{\sigma}^z + 2E_J^A \cos(\frac{\phi_e^A}{2}) \tilde{\sigma}^x. \quad (10)$$

Here we have made use of

$$\begin{aligned} \sum_n (n - n_g)^2 |n\rangle \langle n| &= n_g^2 |0\rangle \langle 0| + (1 - 2n_g + n_g^2) |1\rangle \langle 1| \\ &= \frac{1 - 2n_g}{2} \tilde{\sigma}^z \end{aligned} \quad (11)$$

by dropping the constant term $(n_g^2 + \frac{1-2n_g}{2})(|0\rangle \langle 0| + |1\rangle \langle 1|)$. Hence the qubit Hamiltonian becomes a 2×2 matrix. The gate voltage V_g is the electric potential at the point of the TLR where the qubit couples to. This

includes the DC gate voltage on the qubit and a quantum mode of the TLR:

$$V_g = V^{dc} + \widehat{V}^{ac}. \quad (12)$$

As Figure 1 shows, the qubit is coupled to the center of the TLR so the quantum mode of the voltage is

$$\widehat{V}^{ac} = \frac{2eN}{\sqrt{2C^c}} = V_{rms}(a^\dagger + a) \quad (13)$$

for the fundamental mode, where $V_{rms} = \sqrt{\omega^c/2C^c}$ is the root-mean-square value of the ground state voltage at the center of the TLR. Hence

$$n_g = n^{dc} + C_g^A \sqrt{\omega^c/E_c^c}(a^\dagger + a). \quad (14)$$

For the DC gate voltage bias at the degeneracy point $n^{dc} = \frac{1}{2}$,

$$H^{qubit} = E_c^A C_g^A \sqrt{\omega^c/E_c^c}(a^\dagger + a) \tilde{\sigma}^z + 2E_J^A \cos(\frac{\phi_e^A}{2}) \tilde{\sigma}^x. \quad (15)$$

Using the qubit representation, we obtain

$$\sigma^x = |\uparrow\rangle \langle \downarrow| + |\downarrow\rangle \langle \uparrow| \quad (16)$$

$$\sigma^z = -|\downarrow\rangle \langle \downarrow| + |\uparrow\rangle \langle \uparrow| \quad (17)$$

While biased at the degeneracy point, the eigenbasis of the qubit Hamiltonian is given by $|\uparrow\rangle = (|0\rangle + |1\rangle)/\sqrt{2}$ and $|\downarrow\rangle = (|0\rangle - |1\rangle)/\sqrt{2}$. The combined system for one site now has the following form

$$\begin{aligned} H^{site} &= 2e \frac{C_g^A}{C_\Sigma^A} \sqrt{\omega^c C^c} (a^\dagger + a) \sigma^x + \frac{\omega^q}{2} \sigma^z + \omega^c a^\dagger a \\ &= \omega^c a^\dagger a + \frac{\omega^q}{2} \sigma^z + g^q \sigma^x (a^\dagger + a), \end{aligned} \quad (18)$$

where $\omega^q = 4E_J^A \cos(\frac{\phi_e^A}{2})$.

The magnitudes of the qubit frequency and cavity frequency are in the same range of about 10GHz, so it is natural to apply the rotating wave approximation (RWA). Let $\Delta = \omega^c - \omega^q$ denote the detuning between the cavity and qubit frequencies. Then $\Delta = \omega^c - \omega^q \ll \omega^c + \omega^q$. Moving into the interaction picture and rotating frame one gets the Jaynes-Cummings interaction

$$\begin{aligned} H_{int}^{rot} &= g^q (\sigma_+ e^{i\omega^q t} + \sigma_- e^{-i\omega^q t}) (a^\dagger e^{i\omega^c t} + a e^{-i\omega^c t}) \\ &\stackrel{RWA}{\approx} g^q (\sigma_- a^\dagger e^{i\Delta t} + \sigma_+ a e^{-i\Delta t}), \end{aligned} \quad (19)$$

where the fast oscillation terms with the phase $e^{i(\omega^c + \omega^q)t}$ and $e^{-i(\omega^c + \omega^q)t}$ are neglected in the RWA. Moving back to the non-rotating frame we get the JC Hamiltonian

$$\begin{aligned} H^{site} &= \omega^c a^\dagger a + \frac{\omega^q}{2} \sigma_z + g^q (\sigma_- a^\dagger + \sigma_+ a) \\ &= H_0 + V, \end{aligned} \quad (20)$$

where the diagonal term is $H_0 = \omega^c(a^\dagger a + \sigma^z)$ and the interaction term is $V = \Delta \sigma^z/2 + g^q(\sigma_- a^\dagger + \sigma_+ a)$. Here we

consider the dispersive regime^{28,62} so $\Delta \gg g^q$ and there is no excitation from $|g\rangle$ to $|e\rangle$. Moreover, $g^q(\sigma^- a^\dagger + \sigma^+ a)$ becomes a perturbation term. In order to get higher-order effective interactions we apply the standard perturbation theory to the fourth order and obtain

$$E_g^{(0)} = 0, E_e^{(0)} = \Delta, V_{gg} = V_{ee} = 0, V_{ge} = g^q a^\dagger = V_{ge}^\dagger.$$

Hence we only consider the correction terms for $E_g^{(0)}$.

$$E_g^{(1)} = V_{gg} = 0, \quad (21)$$

$$E_g^{(2)} = -\frac{g^{q2}}{\Delta} aa^\dagger, \quad (22)$$

$$E_g^{(3)} = \frac{V_{ge} V_{ee} V_{eg}}{\Delta^2} = 0, \quad (23)$$

$$E_g^{(4)} = \left(\frac{g^q}{\Delta}\right)^3 g^q a^\dagger aa^\dagger a. \quad (24)$$

Then

$$V = -\frac{g^{q2}}{\Delta} aa^\dagger + \left(\frac{g^q}{\Delta}\right)^3 g^q a^\dagger aa^\dagger a. \quad (25)$$

Here the Kerr term $\left(\frac{g^q}{\Delta}\right)^3 g^q a^\dagger aa^\dagger a$ gives rise to an effective on-site interaction. Going back to the Schrodinger picture, the single-site Hamiltonian becomes

$$H^{site} = (\omega^c - \frac{g^{q2}}{\Delta} + \left(\frac{g^q}{\Delta}\right)^3 g^q) a^\dagger a \quad (26)$$

$$+ \frac{\omega^q}{2} \sigma^z + \left(\frac{g^q}{\Delta}\right)^3 g^q a^\dagger a (a^\dagger a - 1).$$

The charge qubit could be either a single Cooper-pair transistor (SCT) or a transmon^{11,12,14,59} whose qubit frequency can be tuned by changing the magnetic flux bias through a SQUID loop in the qubit circuit. The detuning Δ is a controllable parameter. $\omega^{c,eff} = \omega^c - \frac{g^{q2}}{\Delta} + \left(\frac{g^q}{\Delta}\right)^3 g^q$ is the effective cavity frequency and $U = 2\left(\frac{g^q}{\Delta}\right)^3 g^q$ becomes the effective on-site interaction energy of the photons. Both of them are functions of Δ . Assuming $g^q = 120\text{MHz} \times 2\pi^{13,14}$, $\Delta \geq 0.9\text{GHz} \times 2\pi$ so $(\omega^c - \omega^{c,eff}) \in [-0.1, 0.1]\text{GHz} \times 2\pi$. We remark that the case $\Delta \sim g^q$, where the excitations are polaritons rather than photons, has been discussed in the literature³⁹.

B. Tunable TLR array

Tunable couplings between different sites are necessary in simulating the BHM. Different architectures for implementing a tunable coupler between two superconducting TLRs have been realized and discussed in Refs. 47,48,50–53,58. Here we present a basic design as shown in Figure 1 to demonstrate our quantum simulator. SQUID B with different size and energy from those of SQUID A is used to couple the TLRs. The coupling term is from SQUID B and

$$H^B = \sum_{i=upp,low} \left[-\frac{C_J^B}{2} \left(\dot{\phi}_i^{jj}\right)^2 + E_J^B (1 - \cos \phi_i^{jj}) \right], \quad (27)$$

where $\dot{\phi}_{i=upp,low}^{jj}$ are the phase differences across the upper and lower Josephson junctions of SQUID B (see Fig. 1). By changing of variables $\phi_e^B = \dot{\phi}_{upp}^{jj} + \dot{\phi}_{low}^{jj}$, where ϕ_e^B is the external magnetic flux bias through SQUID B, $\dot{\phi}_{upp}^{jj} + \dot{\phi}_{low}^{jj} = \dot{\phi}_e^B = 0$. Let the node phases on the two ends that connect to TLR 1 and 2 be ϕ_1^c and ϕ_2^c . According to the geometry of the SQUIDS, $\phi_1^c - \phi_2^c = \frac{1}{2}(\dot{\phi}_{upp}^{jj} - \dot{\phi}_{low}^{jj})$ so $\dot{\phi}_{upp}^{jj} - \dot{\phi}_{low}^{jj} = 2(\phi_1^c - \phi_2^c)$. After some algebra, one gets $\left(\dot{\phi}_{upp}^{jj}\right)^2 + \left(\dot{\phi}_{low}^{jj}\right)^2 = 2(\dot{\phi}_1^c)^2 - 4\dot{\phi}_1^c \dot{\phi}_2^c + 2(\dot{\phi}_2^c)^2$. Here we define $N_{1,2}$ as the number of Cooper pairs on the node connected to TLR 1 or 2, so $\frac{C_J^B}{2} \left(\dot{\phi}_{1,2}^c\right)^2 = \frac{1}{2} \frac{(2e)^2}{C_J^B} N_{1,2}^2 = E_c^B N_{1,2}^2$. Therefore the charge energy becomes ($i = upp, low$)

$$\sum_i \frac{C_J^B}{2} \left(\dot{\phi}_i^{jj}\right)^2 = C_J^B (\dot{\phi}_1^c)^2 - 2C_J^B \dot{\phi}_1^c \dot{\phi}_2^c + C_J^B (\dot{\phi}_2^c)^2$$

$$= 2E_c^B N_1^2 - 4E_J^B N_1 N_2 + 2E_c^B N_2^2. \quad (28)$$

We also assume that the two Josephson junctions in SQUID B are uniform. By neglecting some constant terms, the Josephson energy becomes ($i = upp, low$)

$$\sum_i E_J^B (1 - \cos \phi_i^{jj}) = -2E_J^B \cos\left(\frac{\phi_e^B}{2}\right) \cos\left(\frac{\phi_{upp}^{jj} - \phi_{low}^{jj}}{2}\right)$$

$$= -2E_J^B \cos\left(\frac{\phi_e^B}{2}\right) \cos(\phi_1^c - \phi_2^c). \quad (29)$$

It will be shown that $2E_J^B \cos\left(\frac{\phi_e^B}{2}\right)$ can be tuned to the same order of magnitude as the on-site interaction term $\left(\frac{g^q}{\Delta}\right)^3 g^q$ in Eq. (26), which is needed to place the system near the MI-SF phase transition. Moreover, the phase difference $\left(\phi_{upp}^{jj} - \phi_{low}^{jj}\right)$ can initially be set to zero by shorting both sides. Expanding $\cos\left(\frac{\phi_{upp}^{jj} - \phi_{low}^{jj}}{2}\right)$ to the second order, one obtains ($i = upp, low$)

$$\sum_i E_J^B (1 - \cos \phi_i^{jj}) \simeq E_J^B \cos\left(\frac{\phi_e^B}{2}\right) [(\phi_1^c)^2 - 2\phi_1^c \phi_2^c + (\phi_2^c)^2]. \quad (30)$$

Combining Eqs. (28) and (30), one gets the Hamiltonian for SQUID B

$$H^B = \sum_{i=1,2} [2E_c^B N_i^2 + E_J^B \cos\left(\frac{\phi_e^B}{2}\right) (\phi_i^c)^2]$$

$$- [4E_J^B N_1 N_2 + 2E_J^B \cos\left(\frac{\phi_e^B}{2}\right) \phi_1^c \phi_2^c] \quad (31)$$

$$= H_{1,2}^{TLR'} + H^{coup}. \quad (32)$$

Here the simple harmonic terms $H_{1,2}^{TLR'}$ give additional frequency shift to the TLR Hamiltonian in Eq. (4). Since

the net TLR Hamiltonian is

$$\begin{aligned} H_{net,i}^{TLR} &= \frac{1}{2}(E_c^c + 4E_c^B)N_i^2 + \frac{1}{2}[E_L^c + 2E_J^B \cos(\frac{\phi_e^B}{2})](\phi_e^c)^2 \\ &= \frac{1}{2}E_c^{c*}N_i^2 + \frac{1}{2}E_L^{c*}(\phi_e^c)^2, \end{aligned} \quad (33)$$

the dressed cavity frequency becomes

$$\omega^{c*} = 2\pi\sqrt{E_c^{c*}E_L^{c*}}. \quad (34)$$

Once the TLRs are connected into an array with those SQUID Bs, the fundamental cavity frequency changes from ω^c to ω^{c*} . Moreover, TLR 1 and 2 are coupled by

$$\begin{aligned} H^{coup} &= -[4E_J^B N_1 N_2 + 2E_J^B \cos(\frac{\phi_e^B}{2})\phi_1^c \phi_2^c] \\ &= -g^{cap}(a_1^\dagger + a_1)(a_2^\dagger + a_2) \end{aligned} \quad (35)$$

$$+ g^{ind}(a_1^\dagger - a_1)(a_2^\dagger - a_2). \quad (36)$$

Here the coupling constants are

$$\begin{cases} g^{cap} = \frac{\omega^c E_c^B}{E_c^{c*}} \\ g^{ind} = \frac{\omega^c 4E_J^B \cos(\frac{\phi_e^B}{2})}{E_L^{c*}} \end{cases}. \quad (37)$$

A similar coupling Hamiltonian can be found in Ref. 48, which is supported by experiments⁴⁹. By considering two identical resonators $\omega_1^{c*} = \omega_2^{c*}$ and applying the RWA and conservation of the photon number, one obtains

$$H^{coup} \simeq -(g^{cap} + g^{ind})(a_1^\dagger a_2 + a_1 a_2^\dagger) = g(a_1^\dagger a_2 + a_1 a_2^\dagger).$$

The TLR-SQUID-TLR (TST) system has the Hamiltonian

$$H^{TST} = \sum_{i=1,2} \hbar\omega_i^{c*} a_i^\dagger a_i - g(a_1^\dagger a_2 + a_1 a_2^\dagger). \quad (38)$$

We consider typical values^{13,14} of $E_c^B = 300\text{MHz} \times 2\pi$, $E_J^B = 500\text{MHz} \times 2\pi$, $E_c^{c*} = 10\text{GHz} \times 2\pi$, $E_L^{c*} = 10\text{GHz} \times 2\pi$. Note that ϕ_e^B can be tuned within $[0, 2\pi]$, so $g^{ind} \in [2, -2]\text{GHz} \times 2\pi$. The net coupling strength is $g = -(g^{cap} + g^{ind}) \in [-2.3, 1.7]\text{GHz} \times 2\pi$. Since the perturbation approach is applied to the on-site Hamiltonian, in order to keep H^{coup} with the same order of magnitude as the highest order term in Eq. (26), the coupling strength g has to fulfill the condition $g < g^q$. By biasing the system in the range ϕ_e^B around π , one should be able to get a smaller range of $g \in [-30, 30]\text{MHz} \times 2\pi$.

C. Superconducting-circuit simulator of the BHM

Combining the on-site Hamiltonian and couplings between nearest neighbor sites, we obtain a many-body

Jaynes-Cumming Hubbard Hamiltonian:

$$\begin{aligned} H^{JCHM} &= \sum_{i=1}^N [\hbar\omega_i^{c*} - \frac{g_i^q}{\Delta} + (\frac{g_i^q}{\Delta})^3 g_i^q] a_i^\dagger a_i + \sum_{i=1}^N \hbar\omega_i^q \sigma_i^z \\ &+ \sum_{i=1}^N (\frac{g_i^q}{\Delta})^3 g_i^q a_i^\dagger a_i (a_i^\dagger a_i - 1) \\ &- \sum_{i=1}^{N-1} (g_i^{cap} + g_i^{ind})(a_i^\dagger a_{i+1} + a_i a_{i+1}^\dagger) \end{aligned} \quad (39)$$

In the dispersive regime, where our perturbation approach is applicable, the qubit does not get excitations and stays in its ground state. Therefore the qubit term $\sum_{i=1}^N \omega_i^q \sigma_i^z$ does not contribute to the many-body energy.

In this case, the Jaynes-Cummings lattice model can be mapped to the Bose Hubbard model²⁸ by neglecting the qubit term from Eq. (39) and treating the photons in the TLR as interacting bosons.

When compared to Eq. (1), the on-site energy, on-site interaction, and hopping terms are

$$\mu_i = -[\omega_i^{c*} - (\frac{g_i^q}{\Delta})g_i^q + (\frac{g_i^q}{\Delta})^3 g_i^q] \quad (40)$$

$$\frac{U_i}{2} = (\frac{g_i^q}{\Delta})^3 g_i^q \quad (41)$$

$$t_i = (g_i^{cap} + g_i^{ind}) = g_i. \quad (42)$$

As discussed previously, Δ_i and g_i can be tuned by a magnetic flux bias, so they are the independent variables in this model. One may recall that $|t| = |g| \in [0, 30]\text{MHz} \times 2\pi$ from previous discussions. In the dispersive regime $|\Delta| \in [0.9, 1.2]\text{GHz} \times 2\pi$ should give reasonable values^{13,14} of $g^q = 120\text{MHz} \times 2\pi$. Thus $g^q/t \in [4, +\infty)$, $|\Delta/t| \in [30, +\infty)$. In terms of the BHM, $U/t \in (0, +\infty)$, which implies that the range of U/t that can be simulated by this simulator should cover the MISO transition. To avoid going beyond the valid range of our approximation, the parameters are chosen in the range $|\Delta/t| \in [30, 10^3]$.

In this simulation scheme one may notice that the on-site energy μ_i , interaction strength U_i , and hopping coefficient t_i can be explicitly made site-dependent. Therefore, this superconducting TLR array can be a versatile simulator of the BHM, especially if phenomena due to spatial inhomogeneity are of interest. Furthermore, compared to ultracold atoms in optical lattices, this superconducting circuit simulator has some additional features. As we already emphasized, all parameters can be tuned individually and this makes it possible to study problems in various geometries. Moreover, the interacting bosons in the simulator is confined inside the TLRs so there is no need for background trapping potentials, which is common in cold-atom systems. Moreover, open boundary conditions (OBCs) with hard walls can be introduced by terminating the coupling SQUID at the

ends of the superconducting TLR array. Even though weak capacitive couplings to the leads at the two ends of the array may be present, a high Q factor can still be maintained⁴³. On the other hand, periodic boundary conditions (PBCs) can be realized by fabricating a 1D array into a loop structure. Hence bulk properties can be studied with a small number of sites with minimal boundary effects. The examples given in the following sections illustrates those features of the superconducting circuit simulator.

III. SINGLE-SITE MANIPULATIONS OF THE MI-SF TRANSITION

Here we present one interesting application of this superconducting circuit simulator, where the MI-SF transition of the BHM can be induced by single-site manipulations. Other possible applications will be discussed later. To concentrate on the underlying physics, we consider a 1D array of N sites. For simplicity, the parameters of a selected site (called site 1) is tuned by external magnetic flux through the charge qubit coupled to the TLR of this site. One may consider, for site 1, a shift of the onsite energy by δ and a shift of the onsite coupling constant by η . The choice of which site should be manipulated is not important since the conclusions remain the same for the case with PBC. From the BHM (1), the Hamiltonian of this 1D array is rewritten in the form

$$H = \delta n_1 + \eta n_1(n_1 - 1) - \mu \sum_{i=1}^N n_i + \frac{U}{2} \sum_{i=1}^N n_i(n_i - 1) - t \sum_i^{N'} (b_i^\dagger b_{i+1} + b_{i+1}^\dagger b_i), \quad (43)$$

where

$$\begin{cases} \delta = -g_q^2 \left(\frac{1}{\Delta_1} - \frac{1}{\Delta_i} \right) + g_q^4 \left[\left(\frac{1}{\Delta_1} \right)^3 - \left(\frac{1}{\Delta_i} \right)^3 \right] \\ \eta = g_q^4 \left[\left(\frac{1}{\Delta_1} \right)^3 - \left(\frac{1}{\Delta_i} \right)^3 \right] \end{cases}. \quad (44)$$

Here Δ_1 is the detuning energy between the qubit and TLR on the site 1 while Δ_i is the detuning of the other sites. A diagram of δ and η as a function of Δ_1 is shown in Figure 2, which gives an estimation of the BHM parameters in the presence of a single-site manipulation.

In the upper limit of the summation, $N' = N - 1$ is for the OBC while $N' = N$ is for the PBC. We keep $t_i = t$ the same in the whole lattice because it does not depend on Δ_1 . We vary Δ_1/t as an independent variable. The unit of energy will be t . The advantages of this protocol are: (1) The qubit energy is intact away from the manipulated site. (2) Particles are conserved in the whole system. We define the particle density ρ as the ratio between the photon number and site number. In the following we consider the phase transition due to this single-site

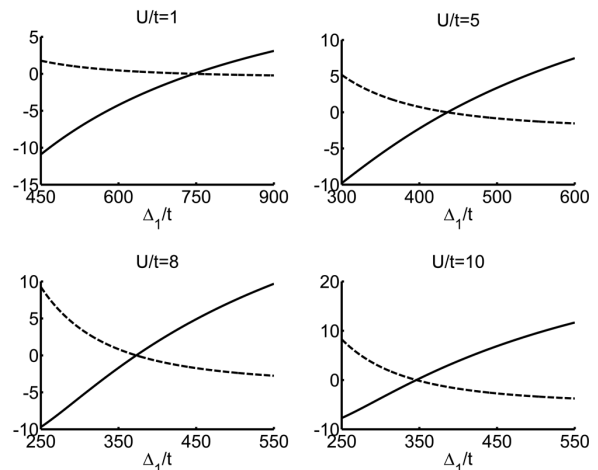


FIG. 2: δ (solid lines) and η (dashed lines) as functions of Δ_1 for $U/t = 1, 5, 8, 10$ and $g^q = 120\text{MHz} \times 2\pi$. As Eq. (43) shows, δ and η are the displacements of the on-site energy and on-site interaction of the first site.

manipulation when $\rho < 1$ and $\rho = 1$. For $\rho = (N - 1)/N$ the system is a delocalized SF state in the absence of manipulations and a single-site push leads to a localized MI state, which is shown schematically in Fig. 3(a)(b). The second case with $\rho = 1$ is illustrated by Fig. 3(c)(d), where the system is in an MI state without manipulations and becomes an SF after a single-site push.

To characterize those single-site manipulated transitions and to identify where the transitions take place, we analyze a useful quantity called the fidelity metric, which has been shown to capture quantum phase transitions or sharp quantum crossovers in fermion Hubbard model^{57,87} and other model Hamiltonians^{56,88}. Given a Hamiltonian of the form $H(\lambda) = H_0 + \lambda H_1$, the fidelity is defined as the overlap between two (renormalized) ground states obtained with a small change $\delta\lambda$ in the parameter λ :

$$F(\lambda, \delta\lambda) = \langle \Phi_0(\lambda) | \Phi_0(\lambda + \delta\lambda) \rangle. \quad (45)$$

However, the fidelity has been shown to be an extensive quantity that scales with the system size^{86,88}. Therefore, the fidelity metric is induced as^{85,87,88}

$$g(\lambda, \delta\lambda) = (2/N)(1 - F(\lambda, \delta\lambda))/\delta\lambda^2, \quad (46)$$

whose limit as $\delta\lambda \rightarrow 0$ is well defined away from the critical points and standard perturbation theories apply. More precisely,

$$\lim_{\delta\lambda \rightarrow 0} g(\lambda, \delta\lambda) = \frac{1}{N} \sum_{\alpha \neq 0} \frac{|\langle \Phi_\alpha(\lambda) | H_1 | \Phi_0(\lambda) \rangle|^2}{[E_0(\lambda) - E_\alpha(\lambda)]^2}. \quad (47)$$

The fidelity metric measures how significantly the ground-state wave function changes as the parameter λ changes. A dramatic increase of the fidelity metric as a function of the varying parameter indicates a quantum phase transition or sharp quantum crossover⁵⁶.

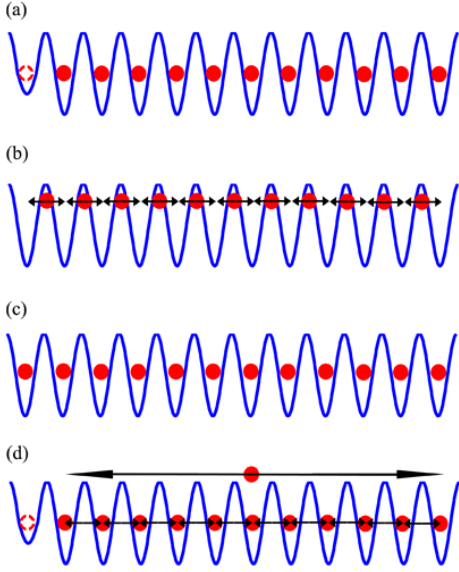


FIG. 3: (a) and (b) illustrate the Mott insulator to superfluid transition for $N - 1$ bosons with strong repulsion in N sites. (a) The on-site energy of site-1 is increased and this pushes the system into a localized Mott insulator phase. The dashed circle means the first site is virtually empty due to its large on-site energy. (b) The system becomes a delocalized superfluid state when the on-site energy is about the same as that of the other sites. (c) and (d) illustrate the transition for N bosons with strong repulsion in N sites. (c) When the array is uniform, the bosons are in a localized Mott insulator phase. (d) By increasing the on-site energy of site 1, photons are pushed into the bulk and form a delocalized superfluid.

A. Case 1: $\rho < 1$

When there are $(N - 1)$ photons in an array of N sites, the ground state should be delocalized due to the incommensurate filling if all the sites have the same on-site energy and interaction energy. As will be shown in Figure 4 and Figure 5, non-uniform distributions of n_i and stronger fluctuations of the on-site photon density, quantified by the variance $\sigma_i = \langle \langle n_i^2 \rangle - \langle n_i \rangle^2 \rangle$, in the small Δ_1 regime indicates delocalization of the photons with interactions up to $U = 10t$. By increasing the on-site energy of site 1, which can be performed by increasing Δ_1 , a transition to a localized MI state of the remaining $N - 1$ sites occurs. The setup is summarized in Figure 3(a)(b). Based on current experimental technology^{6-8,42}, the size of the lattice in our exact diagonalization are chosen as $N = 4, 8, 12$. An estimation of the phase transition point can be obtained from a mean-field approximation.

For a homogeneous 1D array of N sites, the $(N - 1)$ photons are not localized if the hopping coefficient is finite. By increasing the on-site energy of the first site, it becomes unfavorable if any particle hops into it. If the repulsive interactions between the bosons exceed the critical value of the MI-SF transition ($U_c/t \approx 3.28$ in 1D^{54,55}), the ground state for the rest $N - 1$ sites becomes

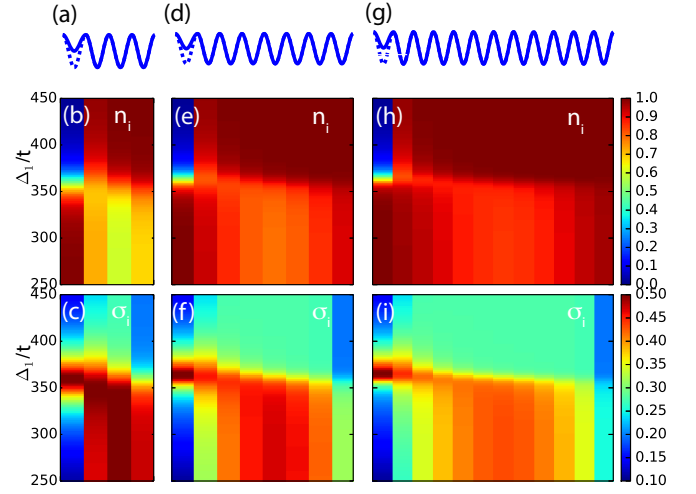


FIG. 4: Exact diagonalization results of the density n_i and its variance σ_i as functions of Δ_1 for Case-1 with OBC. Site 2 to N are uniform and $U = 10t$. (a)-(c) show the results for a 4-site array with 3 photons. In (a) the dashed line and solid line on the first site correspond to the two schemes shown in Fig. 3. (d)-(f) correspond to the case of 8 sites with 7 photons. (g)-(i) correspond to 12 sites with 11 photons.

a Mott insulator with a wavefunction in Fock space as

$$|\varphi_1\rangle = |0, 1, 1, \dots, 1\rangle. \quad (48)$$

By applying this ground state to the Hamiltonian (43), one gets the ground state energy

$$E_1 = \langle \varphi_1 | H | \varphi_1 \rangle = -\mu(N - 1). \quad (49)$$

Then we estimate the ground state of a SF and compare the two ground state energies to determine where the transition occurs when Δ_1 is varied. In our mean-field approximation, we consider a simplified trial ground state with no double occupancy, which is appropriate for the case $U \gg t$. In Fock space, states like $|0, 2, 0, 1, \dots, 1\rangle$ are neglected. Thus the trial ground state is

$$|\varphi_2\rangle = \frac{1}{\sqrt{N}} (|0, 1, 1, \dots, 1\rangle + |1, 0, 1, \dots, 1\rangle + |1, 1, 0, \dots, 1\rangle + \dots + |1, 1, 1, \dots, 0\rangle). \quad (50)$$

The ground state energy is

$$\begin{aligned} E_2 &= \langle \varphi_2 | H | \varphi_2 \rangle \\ &= \frac{1}{N} [-2t(N - 1) - \mu N(N - 1) + (\delta + \eta)(N - 1)] \\ &\approx \delta + \eta - 2t - \mu(N - 1). \end{aligned} \quad (51)$$

The energy difference between the two ground states is

$$\Delta E = E_1 - E_2 \approx 2t - (\delta + \eta). \quad (52)$$

A phase transition occurs at the crossing point $\Delta E = 0$, or $(\delta + \eta) = 2t$. Thus the system forms a Mott insulator by emptying the first site. From Eq. (44) we obtain

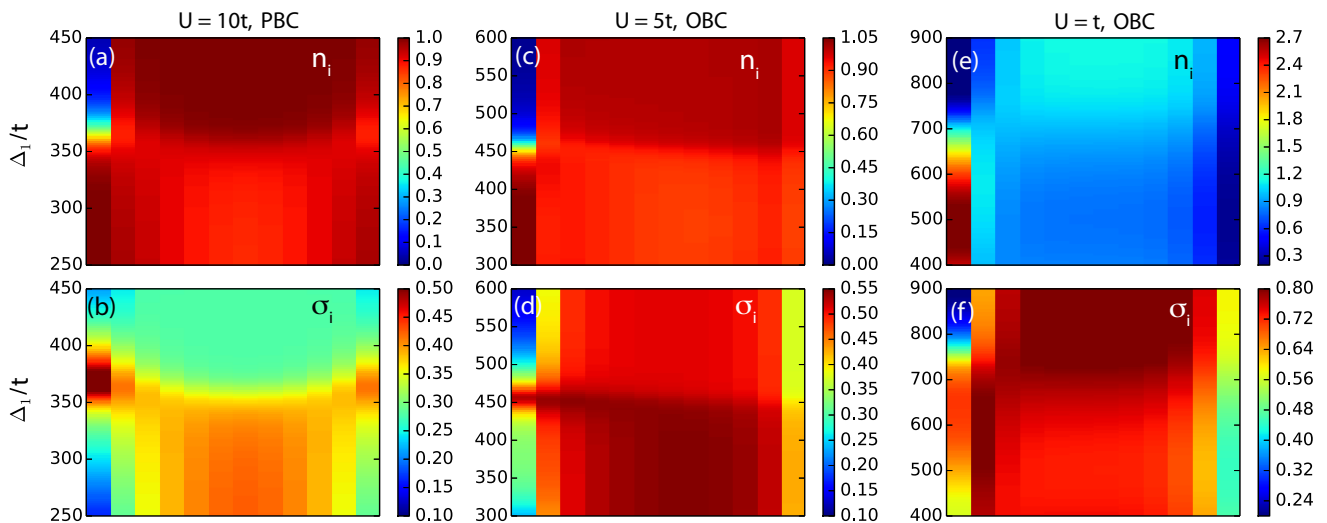


FIG. 5: Photon density profiles and its variance for selected values of U and boundary conditions. (a) and (b): $U/t = 10$ and PBC. In this case, the photons in site 2 and N can both tunnel to site 1. Hence the photon density on site 2 and N are different from the bulk value due to boundary effects. (c) and (d): $U/t = 5$ and OBC. (e) and (f): $U/t = 1$ and OBC. The non-uniform density and its significant variance of the last case indicate that there is no Mott insulator in this setting. Here $N = 12$ with 11 photons.

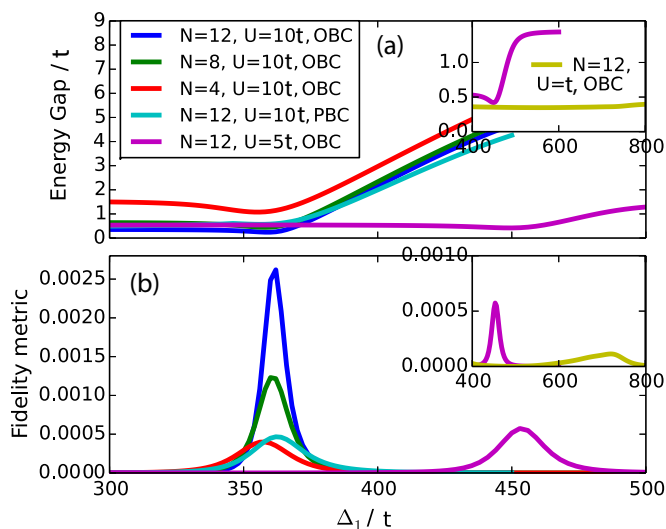


FIG. 6: (a) Energy gap for different values of U and N . The inset shows a regime when $U = t$, in yellow, for $N = 12$ with OBC compared to $U = 5t$ from the main figure. (b) The peaks of Fidelity metric illustrate the critical points. When N varies, the location of the critical point remains intact. However, varying the on-site interaction U changes the location of the critical point, which is consistent with the analysis in Sec. III.

an estimation of the phase transition point at $\Delta_1 \approx 390t$ for $U = 10t$. To check this prediction and provide more accurate estimations, we implement the ED method for several moderate-size systems. Figures 4 and 5 show ground state properties including n_i and σ_i on different sites as Δ_1 varies. The energy gap of the first excited state, shown in Figure 5(a), verifies the existence of the

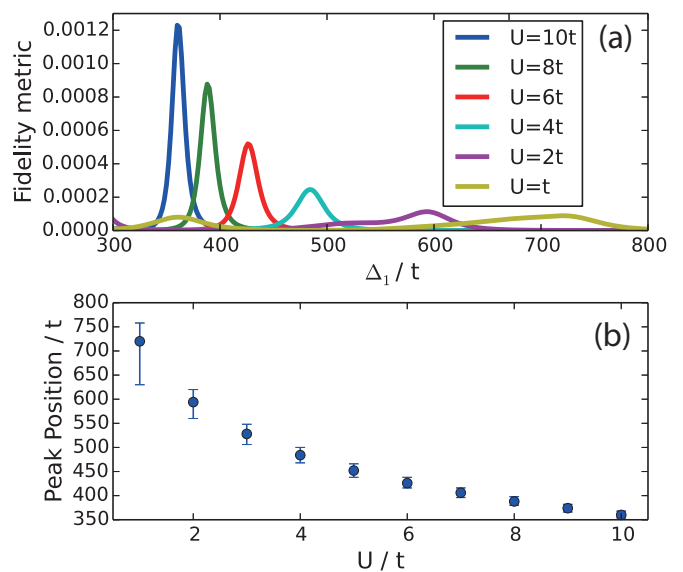


FIG. 7: (a) Fidelity metric as a function of Δ_1 for different values of U for $N = 8$ and 7 photons. (b) Peak position of Fidelity metric as a function of U/t . The full width at half maximum (FWHM) is shown as the bar spanning across each point.

SF (gapless) and MI (gapped) states.

The fidelity metric shown in Figures 5(b) and 6 captures and locates the critical regime when the on-site energy of site 1 is manipulated. In Figure 4, above $\Delta_1/t \approx 365$, the density is uniform away from site 1. The variance σ_i is also suppressed in the bulk. Thus the system is in the MI regime. Below $\Delta_1/t \approx 365$, the photons tend to congregate at the two ends of the array,

but the variance is small. At the center of the array, the photon density is smaller with a larger variance. This corresponds to a delocalized state. The density n_i thus captures the main conclusion of our mean-field analysis, and shows corrections from finite-size effects.

The critical values in the numerical results are close to the mean-field estimations. The location of the critical point does not change much as N changes, but the MI features become more prominent when N increases. Due to finite-size and boundary effects, the edge of the Mott insulator is distorted but the bulk indeed exhibits features such as an integer filling and suppressed fluctuations σ_i . Boundary effects can also be observed on the neighbors of the manipulated site as their values of n_i deviate from the bulk. Those observations are also valid in Figure 5(a)(b), where site 1 is connected to site 2 and site 12 due to PBC.

For small U/t , as shown in Figure 5 and the insets of Figure 6, the SF state dominates the whole parameter space explored in our ED calculations, which confirms that no artifact is induced if the system is in the SF regime. In the insets of Figure 6, the results of a broader range of Δ_1 for the case of $U = t$ is shown and the small smooth gap through out the range of Δ_1 is consistent with a SF state of the case $U = t$ in Figure 5(e)(f).

Figure 6 shows another signature of the phase transition as $\Delta_1/t \approx 365$ for $U = 10t$ when $N = 4, 8$, and 10, as indicated by a minimum in the energy gap followed by a rapid rise. For different values of U/t , Δ_i in the bulk are different according to Eq. (41). Hence the critical point shifts in the Δ_1/t axis according to Eqs. (44) and (52) and this is consistent with the results shown in Figure 6.

B. Case 2: $\rho = 1$

As illustrated in Figure 3(c)(d), here we consider N photons placed in an N -site array. If U/t is large, the system is in a Mott insulator state. As the on-site energy of site 1 increases, the boson in that site is expected to be pushed to the bulk and this should lead to a delocalized state because of the extra boson. Following a similar procedure, we estimate the critical value of Δ_1 that controls δ and η for this case.

The localized MI ground state can be written as

$$|\varphi_1\rangle = |1, 1, 1, \dots, 1\rangle, \quad (53)$$

with the ground state energy

$$E_1 = \langle \varphi_1 | H | \varphi_1 \rangle = \delta - N\mu.$$

We consider a delocalized trial ground state

$$|\varphi_2\rangle = \frac{1}{\sqrt{N-1}} (|0, 2, 1, \dots, 1\rangle + |0, 1, 2, \dots, 1\rangle + \dots + |0, 1, 1, \dots, 2\rangle), \quad (54)$$

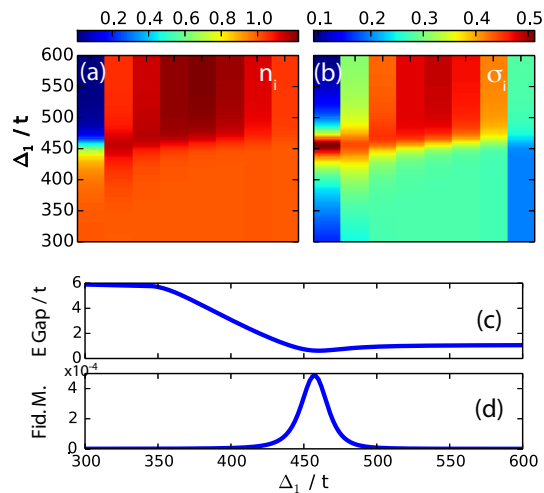


FIG. 8: Exact diagonalization results for Case 2 with $N = 8$ and 8 photons. Here $U = 10t$. (a) and (b) show the density profile in the array and the density variance. The energy gap (E Gap) and fidelity metric (Fid. M.) in (c) and (d) clearly exhibit signatures of the MI-SF transition.

whose ground state energy is

$$\begin{aligned} E_2 &= \langle \varphi_2 | H | \varphi_2 \rangle \\ &= -\frac{(N-1)N}{N-1}\mu + \frac{N-1}{N-1}\frac{U}{2} - \frac{N-2}{N-1}2t \\ &\approx -N\mu + \frac{U}{2} - 2t \end{aligned} \quad (55)$$

Thus the energy difference is

$$\Delta E = E_1 - E_2 \approx \delta - \frac{U}{2} + 2t.$$

The MI-SF phase transition occurs when $\Delta E = 0$, and one may notice that the critical point depends explicitly on U , which is in contrast to the U -independent critical point in the mean-field analysis of case 1. For case 2 we obtain that the critical points are $\delta = 3t, \Delta_1 \approx 469t$ for $U/t = 10$ and $\delta = 0.5t, \Delta_1 \approx 470t$ for $U/t = 5$.

Numerical results from the ED method for this case are shown in Figure 8. As shown in panels (a) and (b), below the critical point $\Delta_1 \sim 470t$, the system is an MI with one photon per site and above $\Delta_1 \sim 470t$ the system becomes an SF with significant σ_i in the bulk. The fidelity metric shown in panel (d) verifies that the critical point is close to the estimation from our mean-field analysis. These results verify the feasibility of inducing and observing those transitions in moderate-sized systems.

IV. IMPLICATIONS FOR EXPERIMENTAL REALIZATION

State Preparation: In the MI regime, the particle density on each site is an integer. One may prepare an arbitrary n -photon state in each site, including $n = 0, 1$

that are of interest, by adiabatically swapping the qubit state to the TLR^{68,69}. This single site preparation can be performed simultaneously on all the sites. Then starting from the MI regime, one can transform it to the many-body ground state for different cases. For example, in case 1 in Sec.III, the ground state in the MI regime is $|0, 1, 1, 1, \dots\rangle$. Recent work also proposes a scheme of a N photon state preparation in a superconducting TLR array supported by numerical results⁴¹.

Cooling: Solid state simulators based on superconducting circuits including the one we propose here contain many degrees of freedom, which not only provide great tunability but also introduce relatively strong couplings to external fields. To experimentally implement the simulator proposed here, cooling such a complex system can be a great challenge. We suggest the following three stages. In stage 1, the whole system is kept in the superconducting phase and thermal excitations in the superconducting circuits and Josephson junctions should be suppressed^{11–15}. They are also associated with suppression of dissipation and decoherence. As mentioned in the introduction, the life time of the photons at this stage is already much longer than the operation time of the superconducting circuit by a factor about 10^7 .

In stage 2, cooling of the TLR-qubit single site system should be performed before connecting the whole array. This is associated with the state preparation of the TLR array and a different degree of freedom from that of stage 1 needs to be dealt with. The quantum computation community has been making significant progresses related to the cooling at this stage¹⁵. Inspired by ideas from optical systems, Sisyphus cooling and side-band cooling of superconducting systems have successfully cooled a qubit to its ground state^{65–67}.

In stage 3, once a multi-site array is connected by turning on the hopping between adjacent sites, the desired many-body Hamiltonian follows. In order to simulate and observe the quantum phase transition discussed here, one needs to constantly cool the system and keep the number of photons conserved during the operation. This is more challenging than cooling just a single site, especially inhomogeneity of the on-site energies is present. Applying a bias or other manipulations of the parameters can cause excitations as well and need to be performed with care. Moreover, to take out the heat from the multi-site system when operating near the critical regime leads to yet another issue. Advanced schemes for cooling a single site have been available while cooling a multi-site array like the one studied here has not been reported so far. Development of such technologies is important for realizing the proposed simulator. Based on current ground-state preparations and state-manipulation technologies developed in coupled superconducting cavity systems^{89,90}, it is promising that photon-number-conserving ground-state cooling processes may be realized by scaling up the cooling methods for those coupled systems.

Detection of phase transition: Since the single-site

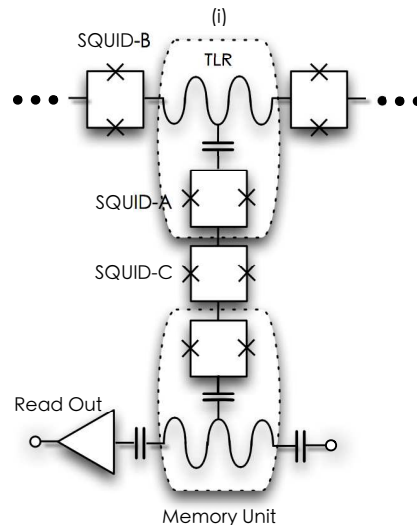


FIG. 9: Measuring the photons in the simulator: Each site of the simulator is connected to a memory unit formed by another qubit-TLR system via a tunable SQUID (labeled as SQUID C) acting as a switch. Measurements of the photon number in the memory unit can be applied^{76–78}. This memory unit can also serve as a circuit for preparing the initial state by manipulating SQUID-C and SQUID-B.

manipulations of the MI-SF transition exhibit strong signatures in the density distribution, we discuss a direct measurement of the photon numbers and number fluctuations on each site. Interestingly, the measurement can be turned on and off when needed. As shown in Figure 9, each site can be coupled to a memory TLR via the additional circuit. The central SQUID-C is used to switch the coupling between the on-site unit and the measurement unit⁷⁹ for controlling the memorizing window. This is possible by changing the bias flux through SQUID-C (labeled on Figure 9), ϕ_m . A fast photon state SWAP between the two TLRs can be applied with four-wave mixing⁶² to get $|n_{on-site} 0_{measure}\rangle \rightarrow |0_{on-site} n_{measure}\rangle$, so that the photons in the TLR of the simulator are transferred and stored into the measurement TLR. Single photon state fast measurements can be applied to measure photon numbers in the memory TLR with technologies developed in circuit QED recently^{70,72,73,76–78}. By repeating the measurement one gets the average photon number $\langle n_i \rangle$ and variation $\langle \sigma_i \rangle$ as depicted in Figure 4 for detecting different quantum phases in the TLR array.

To summarize, a promising way to realize this simulation is: (1) Tune the parameters in the MI regime and prepare the array in the ground state with an integer number of photons. (2) Adiabatically adjust the parameters to the desired values and cool the photons down to their ground state within the photon relaxation time. (3) Measure the photon number in each single site. Then repeat (1) to (3) to obtain the average photon number and number fluctuations.

V. CONCLUSION

A versatile quantum simulator of interacting bosons based on a tunable superconducting TLR-SQUID array has been presented. The BHM with tunable parameters on each site can be studied using the photons in this simulator. We have demonstrated the feasibility of inducing the MI-SF transition by manipulating only one single site. Our results are further supported by the exact diagonalization method, and details of the transition with realistic parameters are presented. The fidelity metric, energy gap, and on-site photon number show signatures of the phase transition. We also discussed possible schemes for state preparation, cooling, and detection of the phase transition for this proposed simulator.

Besides the manipulations of the phase transition discussed here, this quantum simulator is also capable of demonstrating topological properties in the BHM with superlattice structures and should exhibit the topological properties, edge states, and topological phase transitions studied in Refs. 33,34,82. Moreover, quantum quenches^{83,84} and their associated dynamics may also be

simulated by this superconducting circuit simulator as well. For example, similar to Ref. 91 one can separate the TLR array into two sections by turning off the hopping between the two sections. Then different photon numbers are prepared in the two sections. By switching on the hopping between the two sections, photons are expected to slosh back and forth between the two sections, which should be detectable with similar measurement methods. Thus the superconducting circuit simulator adds more excitement to the physics of interacting bosons and complements other available simulators.

VI. ACKNOWLEDGMENTS

We thank Lin Tian and Raymond Chiao for valuable advice on this work and Kevin Mitchell and Jay Sharping for useful discussions. The computations were performed using the resources of the National Energy Research Scientific Computing Center (NERSC) supported by the U.S. Department of Energy, Office of Science, under Contract No. DE-AC02-05CH11231.

-
- * Electronic address: cchien5@ucmerced.edu
- ¹ R. Blatt and C. F. Roos, Nat. Phys. **8**, 277 (2012).
 - ² I. Bloch, J. Dalibard and S. Nascimbène, Nat. Phys. **8**, 267 (2012).
 - ³ A. Aspuru-Guzik and P. Walther, Nat. Phys. **8**, 285 (2012).
 - ⁴ P. Schindler, M. Müller, D. Nigg, J. T. Barreiro, E. A. Martinez, M. Hennrich, T. Monz, S. Diehl, P. Zoller and R. Blatt, Nat. Phys. **9**, 361 (2013).
 - ⁵ J. Cai, A. Retzker, F. Jelezko and M. B. Plenio, Nat. Phys. **9**, 168 (2013).
 - ⁶ A. A. Houck, H. E. Türeci and J. Koch, Nat. Phys. **8**, 292 (2012).
 - ⁷ J. E. Mooij and G. Schön in *Coherence in Superconducting Networks* Vol. **152**(eds Mooij, J. E. and Schön, G.) (NATO Proceedings, North-Holland, 1988).
 - ⁸ R. Fazio and H. van der Zant, Phys. Rep. **355**, 235 (2001).
 - ⁹ C. Bruder, R. Fazio and G. Schön, Ann. Phys. (Leipzig) **14**, 566 (2005).
 - ¹⁰ I. M. Georgescu, S. Ashhab and F. Nori, Rev. Mod. Phys. **86**, 153 (2014).
 - ¹¹ Y. Makhlin, G. Schön and A. Shnirman, Rev. Mod. Phys. **73**, 357 (2001).
 - ¹² M. H. Devoret and J. M. Martinis, Quantum Inf. Process. **3**, 163 (2004).
 - ¹³ M. H. Devoret and R. J. Schoelkopf, Science **339**, 1169 (2013).
 - ¹⁴ J. Clarke and F. K. Wilhelm, Nature (Nature) **453**, 1031 (2008).
 - ¹⁵ J. Q. You and F. Nori, Nature **474**, 589 (2011).
 - ¹⁶ R. Barends, J. Kelly, A. Megrant, A. Veitia, D. Sank, E. Jeffrey, T. C. White, J. Mutus, A. G. Fowler, B. Campbell, Y. Chen, Z. Chen, B. Chiaro, A. Dunsworth, C. Neill, P. O'Malley, P. Roushan, A. Vainsencher, J. Wenner, A. N. Korotkov, A. N. Cleland and J. M. Martinis, Nature **508**, 500 (2014).
 - ¹⁷ J. M. Chow, J. M. Gambetta, E. Magesan, D. W. Abraham, A. W. Cross, B. R. Johnson, N. A. Masluk, C. A. Ryan, J. A. Smolin, S. J. Srinivasan and M. Steffen, Nat. Comm. **5**, 4015 (2014).
 - ¹⁸ A. van Oudenaarden and J. E. Mooij, Phys. Rev. Lett. **76**, 4947 (1996).
 - ¹⁹ M. P. A. Fisher, P. B. Weichman, G. Grinstein, and D. S. Fisher, Phys. Rev. B **40**, 546 (1989).
 - ²⁰ E.T. Jaynes and F. W. Cummings, Proc. IEEE **51**, 89 (1963).
 - ²¹ D. G. Angelakis, M. F. Santos and S. Bose, Phys. Rev. A **76**, 031805 (2007).
 - ²² M. J. Hartmann, F. G. S. L. Brand and M. B. Plenio, Nat. Phys. **2**, 849 (2006).
 - ²³ W. S. Bakr, J. I. Gillen, A. Peng, S. Fölling and M. Greiner, Nature **462**, 74 (2009).
 - ²⁴ W. S. Bakr, A. Peng, M. E. Tai, R. Ma, J. Simon, J. I. Gillen, S. Fölling, L. Pollet and M. Greiner, Science **329**, 547 (2010).
 - ²⁵ A. D. Greentree, C. Tahan, J. H Cole, and L. C L Hollenberg, Nat. Phys. **2**, 856 (2006).
 - ²⁶ M. J. Hartmann and M. B. Plenio, Phys. Rev. Lett. **99**, 103601 (2007).
 - ²⁷ M. J. Hartmann, F. Brandão, and M. Plenio, Laser Photonics Rev. **2**, 527 (2008).
 - ²⁸ J. Koch and K. Le Hur, Phys. Rev. A **80**, 023811 (2009).
 - ²⁹ A. A. Houck, D. I. Schuster, J. M. Gambetta, J. A. Schreier, B. R. Johnson, J. M. Chow, L. Frunzio, J. Majer, M. H. Devoret, S. M. Girvin and R. J. Schoelkopf, Nature **449**, 328 (2007).
 - ³⁰ A. Blais, R.-S. Huang, A. Wallraff, S. M. Girvin and R. J. Schoelkopf, Phys. Rev. A **69**, 062320 (2004).
 - ³¹ L. S. Bishop, J. M. Chow, J. Koch, A. A. Houck, M. H. Devoret, E. Thuneberg, S. M. Girvin, and R. J. Schoelkopf, Nat. Phys. **5**, 105 (2009).

- ³² S. Schmidt and J. Koch, *Annalen der Physik*, **525**, 395 (2013).
- ³³ S.-L. Zhu, Z.-D. Wang, Y.-H. Chan and L.-M. Duan, *Phys. Rev. Lett.* **110**, 075303 (2013).
- ³⁴ M. Atala, M. Aidelsburger, J. T. Barreiro, D. Abanin, T. Kitagawa, E. Demler and I. Bloch, *Nat. Phys.* **9**, 795 (2013).
- ³⁵ D. Jaksch, C. Bruder, J. I. Cirac, C. W. Gardiner and P. Zoller, *Phys. Rev. Lett.* **81**, 3108 (1998).
- ³⁶ S.-K. Choi, D.-H. Lee, S. G. Louie and J. Clarke, *Phys. Rev. Lett.* **103**, 197001 (2009).
- ³⁷ O. Viehmann, J. von Delft and F. Marquardt, *Phys. Rev. Lett.* **110**, 030601 (2013).
- ³⁸ J. Q. You, Z. D. Wang, W. Zhang and F. Nori, *Sci. Rep.* **4**, 5535 (2014).
- ³⁹ M. Leib and M. J. Hartmann, *New J. Phys.* **12**, 093031 (2010).
- ⁴⁰ M. Leib, F. Deppe, A. Marx, R. Gross and M. J. Hartmann, *New J. Phys.* **14**, 075024 (2012).
- ⁴¹ K. Seo, L. Tian, arXiv:1408.2304 [quant-ph].
- ⁴² D. L. Underwood, W. E. Shanks, J. Koch and A. A. Houck, *Phys. Rev. A* **86**, 023837 (2012).
- ⁴³ H. Wang, M. Hofheinz, J. Wenner, M. Ansmann, R. C. Bialczak, M. Lenander, Erik Lucero, M. Neeley, A. D. O'Connell, D. Sank, M. Weides, A. N. Cleland and J. M. Martinis, *Appl. Phys. Lett.* **95**, 233508 (2009).
- ⁴⁴ H. Paik, D. I. Schuster, L. S. Bishop, G. Kirchmair, G. Catelani, A. P. Sears, B. R. Johnson, M. J. Reagor, L. Frunzio, L. I. Glazman, S. M. Girvin, M. H. Devoret and R. J. Schoelkopf, *Phys. Rev. Lett.* **107**, 240501 (2011).
- ⁴⁵ M. Reagor, H. Paik, G. Catelani, L. Sun, C. Axline, E. Holland, I. M. Pop1, N. A. Masluk, T. Brecht, L. Frunzio, M. H. Devoret, L. Glazman and R. J. Schoelkopf, *Appl. Phys. Lett.* **102**, 192604 (2013).
- ⁴⁶ C. Rigetti, J. M. Gambetta, S. Poletto, B. L. T. Plourde, J. M. Chow, A. D. Córcoles, J. A. Smolin, S. T. Merkel, J. R. Rozen, G. A. Keefe, M. B. Rothwell, M. B. Ketchen and M. Steffen, *Phys. Rev. B* **86**, 100506(R) (2012).
- ⁴⁷ J.-Q. Liao, J.-F. Huang, Y.-X. Liu, L.-M. Kuang and C.-P. Sun, *Phys. Rev. A* **80**, 014301 (2009).
- ⁴⁸ B. Peropadre, D. Zueco, F. Wulfschneider, F. Deppe, A. Marx, R. Gross and J. J. García-Ripoll, *Phys. Rev. B* **87**, 134504 (2013).
- ⁴⁹ A. Baust, E. Hoffmann, M. Haeberlein, M. J. Schwarz, P. Eder, E. P. Menzel, K. Fedorov, J. Goetz, F. Wulfschneider, E. Xie, L. Zhong, F. Quijandria, B. Peropadre, D. Zueco, J.-J. Garcia Ripoll, E. Solano, F. Deppe, A. Marx and R. Gross, arXiv:1405.1969.
- ⁵⁰ R. C. Bialczak, M. Ansmann, M. Hofheinz, M. Lenander, E. Lucero, M. Neeley, A. D. O'Connell, D. Sank, H. Wang, M. Weides, J. Wenner, T. Yamamoto, A. N. Cleland and J. M. Martinis, *Phys. Rev. Lett.* **106**, 060501 (2011).
- ⁵¹ R. A. Pinto, A. N. Korotkov, M. R. Geller, V. S. Shumeiko and J. M. Martinis, *Phys. Rev. B* **82**, 104522 (2010).
- ⁵² Y. Chen, C. Neill, P. Roushan, N. Leung, M. Fang, R. Barends, J. Kelly, B. Campbell, Z. Chen, B. Chiaro, A. Dunswoth, E. Jeffrey, A. Megrant, J. Y. Mutus, P. J. J. O'Malley, C. M. Quintana, D. Sank, A. Vainsencher, J. Wenner, T. C. White, M. R. Geller, A. N. Cleland and J. M. Martinis, arXiv:1402.7367.
- ⁵³ S. J. Srinivasan, A. J. Hoffman, J. M. Gambetta, and A. A. Houck, *Phys. Rev. Lett.* **106**, 083601 (2011).
- ⁵⁴ I. Danshita and A. Polkovnikov, *Phys. Rev. A* **84**, 063637 (2011).
- ⁵⁵ S. Ejima, H. Fehske, and F. Gebhard, *Europhys. Lett.* **93**, 30002 (2011).
- ⁵⁶ M. Rigol, B. S. Shastry and S. Haas, *Phys. Rev. B* **79**, 052502 (2009).
- ⁵⁷ C.-J. Jia, B. Moritz, C.-C. Chen, B. S. Shastry and T. P. Devereaux, *Phys. Rev. B* **84**, 125113 (2011).
- ⁵⁸ J.-Q. Liao, J.-F. Huang, Y.-X. Liu, L.-M. Kuang and C. P. Sun, *Phys. Rev. A* **80**, 014301 (2009).
- ⁵⁹ J. Koch, T. M. Yu, J. Gambetta, A. A. Houck, D. I. Schuster, J. Majer, A. Blais, M. H. Devoret, S. M. Girvin and R. J. Schoelkopf, *Phys. Rev. A* **76**, 042319 (2007).
- ⁶⁰ Z. Kim, B. Suri, V. Zaretsky, S. Novikov, K. D. Osborn, A. Mizel, F. C. Wellstood and B. S. Palmer, *Phys. Rev. Lett.* **106**, 120501 (2011).
- ⁶¹ X.-H. Deng, Y. Hu and L. Tian, *Supercond. Sci. Technol.* **26**, 114002 (2013).
- ⁶² A. V. Sharypov, X.-H. Deng, and L. Tian *Phys. Rev. B* **86**, 014516 (2012).
- ⁶³ R. W. Boyd, *Nonlinear Optics* (3ed., Elsevier Inc., 2008).
- ⁶⁴ J.-M. Zhang and R.-X. Dong, *Eur. J. Phys.* **31**, 591 (2010).
- ⁶⁵ M. Grajcar, S. H. W. van der Ploeg, A. Izmalkov, E. Il'ichev, H.-G. Meyer, A. Fedorov, A. Shnirman and G. Schön, *Nat. Phys.* **4**, 612 (2008).
- ⁶⁶ S. O. Valenzuela, W. D. Oliver, D. M. Berns, K. K. Berggren, L. S. Levitov and T. P. Orlando, *Science* **314**, 1589 (2006).
- ⁶⁷ J. Q. You, Y.-X. Liu and F. Nori, *Phys. Rev. Lett.* **100**, 047001 (2008).
- ⁶⁸ A. Wallraff, D. I. Schuster, A. Blais, L. Frunzio, R.-S. Huang, J. Majer, S. Kumar, S. M. Girvin and R. J. Schoelkopf, *Nature* **431**, 162 (2004).
- ⁶⁹ M. Hofheinz, H. Wang, M. Ansmann, R. C. Bialczak, E. Lucero, M. Neeley, A. D. O'Connell, D. Sank, J. Wenner, J. M. Martinis and A. N. Cleland, *Nature* **459**, 546 (2009).
- ⁷⁰ D. Bozyigit, C. Lang, L. Steffen, J. M. Fink, C. Eichler, M. Baur, R. Bianchetti, P. J. Leek, S. Filipp, M. P. da Silva, A. Blais and A. Wallraff, *Nat. Phys.* **7**, 154 (2011).
- ⁷¹ S. Kumar and D.P. DiVincenzo, *Phys. Rev. B* **82**, 014512 (2010).
- ⁷² B. R. Johnson, M. D. Reed, A. A. Houck, D. I. Schuster, L. S. Bishop, E. Ginossar, J. M. Gambetta, L. DiCarlo, L. Frunzio, S. M. Girvin and R. J. Schoelkopf, *Nat. Phys.* **6**, 663 (2010).
- ⁷³ C. Deng, J. M. Gambetta and A. Lupascu, *Phys. Rev. B* **82**, 220505 (2010).
- ⁷⁴ N. Bergeal, R. Vijay, V. E. Manucharyan, I. Siddiqi, R. J. Schoelkopf, S. M. Girvin and M. H. Devoret, *Nat. Phys.* **6**, 296 (2010).
- ⁷⁵ L. DiCarlo, M. D. Reed, L. Sun, B. R. Johnson, J. M. Chow, J. M. Gambetta, L. Frunzio, S. M. Girvin, M. H. Devoret and R. J. Schoelkopf, *Nature (London)* **467**, 574 (2010).
- ⁷⁶ C. Lang, C. Eichler, L. Steffen, J. M. Fink, M. J. Woolley, A. Blais and A. Wallraff, *Nat. Phys.* **9**, 345 (2013).
- ⁷⁷ D. Ristè M. Dukalski, C. A. Watson, G. de Lange, M. J. Tiggelman, Y. M. Blanter, K. W. Lehnert, R. N. Schouten and L. DiCarlo, *Nature (London)* **502**, 350 (2013).
- ⁷⁸ Y. Yin, Y. Chen, D. Sank, P. J. J. O'Malley, T. C. White, R. Barends, J. Kelly, E. Lucero, M. Mariani, A. Megrant, C. Neill, A. Vainsencher, J. Wenner, A. N. Korotkov, A. N. Cleland, and J. M. Martinis, *Phys. Rev. Lett.* **110**, 107001 (2013).
- ⁷⁹ A. O. Niskanen, K. Harrabi, F. Yoshihara, Y. Nakamura, S. Lloyd, and J. S. Tsai, *Science* **316**, 723 (2007).

- ⁸⁰ C. N. Yang, *Rev. Mod. Phys.* **34**, 694 (1962).
- ⁸¹ O. Penrose and L. Onsager, *Phys. Rev.* **104**, 576 (1956).
- ⁸² F. Grusdt, M. Hönig, and M. Fleischhauer, *Phys. Rev. Lett.* **110**, 260405 (2013).
- ⁸³ A. Polkovnikov, K. Sengupta, A. Silva and M. Vengalattore, *Rev. Mod. Phys.* **83**, 863 (2011).
- ⁸⁴ M. A. Cazalilla, R. Citro, T. Giamarchi, E. Orignac and M. Rigol, *Rev. Mod. Phys.* **83**, 1405 (2011).
- ⁸⁵ P. Zanardi and N. Paunkovic, *Phys. Rev. E* **74**, 031123 (2006).
- ⁸⁶ W.-L. You, Y.-W. Li and S.-J. Gu, *Phys. Rev. E* **76**, 022101 (2007).
- ⁸⁷ L. Campos Venuti, M. Cozzini, P. Buonsante, F. Massel, N. Bray-Ali and P. Zanardi, *Phys. Rev. B* **78**, 115410 (2008).
- ⁸⁸ L. Campos Venuti and P. Zanardi, *Phys. Rev. Lett.* **99**, 095701 (2007).
- ⁸⁹ M. Mariani, H. Wang, R. C. Bialczak, M. Lenander, E. Lucero, M. Neeley, A. D. O'Connell, D. Sank, M. Weides, J. Wenner, T. Yamamoto, Y. Yin, J. Zhao, J. M. Martinis, and A. N. Cleland, *Nat. Phys.* **7**, 287 (2011).
- ⁹⁰ Y. Chen, P. Roushan, D. Sank, C. Neill, E. Lucero, M. Mariani, R. Barends, B. Chiaro, J. Kelly, A. Megrant, J. Y. Mutus, P. J. J. O'Malley, A. Vainsencher, J. Wenner, T. C. White, Y. Yin, A. N. Cleland, and J. M. Martinis, arXiv:1403.6808 [cond-mat.supr-con].
- ⁹¹ C. C. Chien, M. Di Ventra, and M. Zwolak, *Phys. Rev. A* **90**, 023624 (2014).